Northumbria Research Link

Conformally anodizing hierarchical structure in a deformed tube towards energy-saving liquid transportation

Wei Li [a,1], Honghao Zhou [b,1], Kaiqi Zhao [a], Jian Jin [a], Xue Chen [b], Muhammad Wakil Shahzad [b], Yinzhu Jiang [c], Omar K. Matar [d,*], Sheng Dai [e,*], Ben Bin Xu [b,*], Lidong Sun [a,*]

[a] State Key Laboratory of Mechanical Transmission, School of Materials Science and Engineering, Chongqing University, Chongqing 400044, PR China
[b] Department of Mechanical and Construction Engineering, Faculty of Engineering and Environment, Northumbria University, Newcastle upon Tyne NE1 8ST, UK
[c] School of Materials Science and Engineering, State Key Laboratory of Clean Energy Utilization, Zhejiang University, Hangzhou, Zhejiang 310027, PR China
[d] Department of Chemical Engineering, Imperial College London, London SW7 2AZ, UK
[e] Department of Chemical Engineering, Brunel University London, Uxbridge UB8 2DW, UK

ARTICLE INFO

ABSTRACT

The creation of drag-reducing surfaces in deformed tubes is of vital importance to thermal management, energy, and environmental applications. However, it remains a great challenge to tailor the surface structure and wettability inside the deformed tubes of slim and complicated feature. Here, we describe an electrochemical anodization strategy to achieve uniform and superhydrophobic coating of TiO_2 nanotube arrays throughout the inner surface in deformed/bend titanium tubes. Guided by a hybrid carbon fibre cathode, conformal electric field can be generated to adaptively fit the complex geometries in the deformed tube, where the structural design with rigid insulating beads can self-stabilize the hybrid cathode at the coaxial position of the tube with the electrolyte flow. As a result, we obtain a superhydrophobic coating with a water contact angle of 157° and contact angle hysteresis of less than 10°. Substantial drag reduction can be realised with an overall reduction up to 25.8 % for the anodized U-shaped tube. Furthermore, we demonstrate to spatially coat tubes with complex geometries, to achieve energy-saving liquid transportation. This facile coating strategy has great implications in liquid transport processes with the user-friendly approach to engineer surface regardless of the deformation of tube/pipe.

1. Introduction

The deformed tubes, such as bend, T-junction and spiral tubes, are ubiquitous components that serve a variety of engineering purposes, e. g., space-saving and/or increasing the contact area in a wide spectrum of applications such as heat exchanger design [1–3], sea water desalination plant [4,5], and advanced immersion cooling system [6], etc. The drag of flow at the liquid/solid interface plays critical role in determining operation cost. There have been a number of advances in the use of superhydrophobic surfaces to reduce drag in liquid transportation [7–9]. A slip boundary condition has been frequently used in most approaches, where a liquid does not penetrate into the surface texture of an immersed superhydrophobic surface [10,11] and locally recirculating air flow can be created by the textures thus lubricating the solid surface

[12–17]. The concept has been applied to transport liquid where surface textures have been widely utilised to minimise drag for the liquid [18–20].

Compared with a straight tube, the pressure drops caused by frictional drag in a deformed tube, e.g., a U-shaped tube [21], can yield significant energy consumption. Meanwhile, the conventional technologies to achieve superhydrophobic surface such as photolithography [20], aerogel [22], plasma treatment [23], and spray coating [24], are less favourable for deformed tubes due to geometrical limitation. Notably, some attempts have been made to coat the inner surface of tubes for drag reduction. Watanabe *et al.* reported 14% drag reduction in the laminar flow range with a water-repellent circular pipe, which was coated with fluorine alkane modified acrylic resin [25]. Yuan *et al.* fabricated superhydrophobic glass tubes and observed non-sticking

motion of water droplets in the tubes [26]. Lv and Zhang reported superhydrophobic aluminium tubes for enhanced drag reduction by chemical etching [27]. Nonetheless, the approaches are generally based on dip coating or solution reactions, thus giving rise to great difficulty in controlling the coating uniformity at the inner surface especially for deformed tubes. The search for an energy saving liquid transportation in a deformed tube with a low cost is an ongoing mission.

Electrochemical anodization can coat a surface under an electric field regardless of surface morphology. Sun *et al.* studied the effect of cathode arrangement on the coating quality for Ti tubes and explored the essential role of electric fields in nanotube growth [28]. We previously developed a coaxial anodization method that can lead to uniform and superhydrophobic coatings on both inner or outer surfaces of straight tubes [29–31]. Despite of the above progresses, considerable challenges remain on how to uniformly coat the inner surface of a deformed tube with desirable wettability. The deformation, e.g., bend tubes, easily leads to either a misalignment of the cathode off the axial position of the tube which in turn causes a nonuniform distribution of the coating layer, or a failure (short circuit) for the anodization induced by a direct contact between the cathode and the tube.

In this work, we develop an electrochemical anodization approach to conformally coat the inner surface of a deformed tube with homogeneous and superhydrophobic layer, regardless of tube geometry, e.g., bending angles, shapes, etc. This process is facilitated by a gauged carbon fibre cathode to offer a coaxial anodization inside the tube once deployed, where a self-stabilization for this hybrid electrode is fulfilled by the design thus ensuring a uniform distribution of the electric field for anodization. Moreover, the anodized conformal hierarchical structure leads to a substantial drag reduction for liquid transportation upon superhydrophobic treatment. This adaptative coating approach provides a practical engineering solution to overcome the structural confinement of tube, in a spatially operational and cost-effective fashion.

2. Experimental section

2.1. Materials and anodization

Seamless titanium tubes with a variety of bending angles were used with configurations as follows: 99.6% purity, 8 mm inner diameter, 1 mm wall thickness, and 157 mm curved length with two straight arms of 100 mm each. The tubes were ultrasonically cleaned in detergent, tap water, ethanol, and deionized water for 20 min in sequence, then dried with nitrogen stream. The electrochemical anodization was carried out in ethylene glycol (anhydrous, 99.8%, Sigma-Aldrich) consisting of 0.3 wt% ammonium fluoride (98%, Sigma-Aldrich) and 2 vol% deionized water at 20 V (Keithley 2200 SourceMeter) and room temperature (20 °C). The electrolyte preparation and pre-treatment were the same as previous practiced in our lab [32]. The titanium tube was used as the anode and the hybrid carbon fibre (diameter: 1 mm, resistivity: 0.17 Ω·m) as the cathode with a number of rigid insulating gauge beads (diameter: 6 mm) decorating the fibre to facilitate anodization. The electrochemical anodization consisted of two stages: Stage I, an electrochemical etching process in 0.1 M sodium chloride aqueous solution at 15 V and room temperature for 2 h, to create the structure roughness in microscale throughout the inner wall. In Stage II, the designed electrolyte solution was introduced with a controlled flow rate by a peristaltic pump, to initiate the nano-structure on the surface. At the end, the tubes were rinsed with deionized water and dried at 50 °C in air. The resulting nanotube coatings were annealed at 450 °C for 3 h to crystalize into anatase structure before any further treatment and application. For superhydrophobic surface, the well-tailored Ti tubes were treated with ethanol solution (anhydrous, 99.9%, Sigma-Aldrich) containing 2 vol% 1H,1H,2H,2H-Perfluorodecyltriethoxysilane (PTES, 97%, Adamas reagent) at 60 °C for 30 min and then dried at 110 °C for 1 h.

2.2. Characterization

Surface and cross-sectional views of the nanotubes were examined by field-emission scanning electron microscopy (FESEM, FEI Nova 400 FEG-SEM). Water contact angle measurements were performed under an optical tensiometer (Attension Theta, Biolin Scientific) equipped with a high-speed digital camera. A water droplet $\sim$ 7 μL was used for the contact angle measurement and to track the droplet sliding. The trajectories of droplet motion and the rest surface drag reduction testing & demonstration were recorded by a digital camera (Nikon Coolpix S7000).

2.3. Theoretical analysis and finite element simulation

The electrolyte flow induced deflection can be defined as a transverse force F on the rigid bead and the carbon fibre, which can be calculated using the following well-known deflection formula for cantilever:

$$u_y(x) = \frac{Fx^2}{6EI}(3L - x) \tag{1}$$

where $\times$ is the coordinate along fibre axis, E is the elastic modulus of carbon fibre, I is the second moment of area for the carbon fibre, and $L = \frac{1}{2}d + \frac{1}{2}\varphi_b$, with d being the distance between two beads and φ_b being the bead diameter (see Fig. 1c). Knowing that the carbon fibre has a circular cross-section with diameter φ_f, we have: $I = 4\pi\varphi_f^4$. The maximum deflection, i.e., the deflection at the end where F is applied, can be found from Eq. (1) as:

$$\text{Max}u_y = u_y(x = L) = \frac{F}{12\pi E\varphi_f^4}L^3 \tag{2}$$

By normalizing Equation (2), we have:

$$\text{Max}\bar{u}_y = \frac{\text{Max}u_y}{\varphi_t} = cL^3 \tag{3}$$

with $c = \frac{F}{12\pi E\varphi_f^4 \varphi_t}$, where φ_t is the diameter of the Ti tube (see Fig. 1c). The transverse force (lift force) F can be estimated by hydrodynamics as:
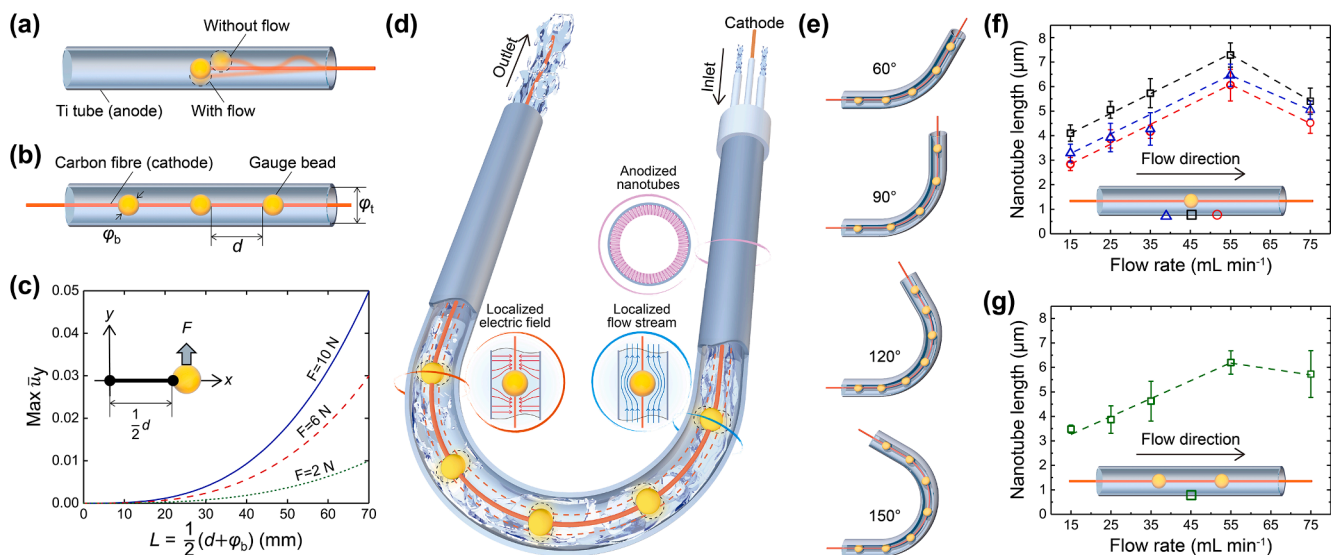
$$F = \frac{1}{2}\rho v^2 SC_L \tag{4}$$

where ρ and v are respectively the density and velocity of the electrolyte solution, S ($= \frac{1}{4}\pi\varphi_b^2$) is projected area of the bead, and C_L is a dimensionless lift coefficient. By taking $\rho = 1\text{g/cm}^3$ (water) and v is the flow speed for the electrolyte solution.

The commercial finite element software ANSYS Fluent was used to simulate the fluid transportation and liquid–solid interaction. Simulations were conducted on 2D tubes in straight shape and bending angles from 30° to 180°. The same length of 350 mm was set for all tubes to ensure equal travel distance of water through tubes. Different surface conditions of tubes were simulated by applying different levels of shear stress on the tube surface, i.e., 5 Pa for the original surface and 0 Pa for the anodized hydrophobic surface. Moreover, to mimic the syringe injection in the experiment, a small rectangular block (1.5 mm × 2 mm) at the tube inlet part was introduced in the simulation and water was injected from this block into the tube. The water inlet velocity was set to be 3 m/s for the stream testing on surface drag, in line with the experimental data of 27.4 mL min^{-1}. Multiphase model was adopted and transient simulation was conducted. Time evolutions of mass flow rate at inlet and outlet and phase diagram showing volume fractions of water and air were obtained from the simulation.

3. Results and discussion

The key concept of coaxial anodization is to electrochemically generate a uniform coating layer inside the deformed tube by utilising a

Fig. 1. Concept and mechanism of coaxial anodization in a deformed tube. a) Drifting of cathode with single bead. b) Stabilisation of hybrid cathode with rigid beads at the presence of liquid flow. c) Normalized maximum deflection of hybrid cathode *versus* L during the anodization. d) Schematic illustration of the electrochemical anodization setup with rigid beads gauged carbon fibre cathode, distribution of streamline and anodized nanolayer in a U-shaped tube and e) tubes with various bending degrees. f) Length of TiO₂ nanotubes grown in the vicinity of an insulating bead and g) that between two beads under different flow rates at 20 V for 8 h. Insets correspond to illustrations showing the positions.

plastic gauge bead decorated carbon fibre cathode, which can self-stabilize at the axial position with a fixed end by following the flow direction (Fig. 1a and 1b). The gauged carbon fibre cathode consists of a conductive and flexible carbon fibre ($\varphi_f = 1$ mm) dressed by a number of rigid insulating plastic beads ($\varphi_b = 6$ mm).

A theoretical analysis is performed to understand this effect (see *Experimental section*) by deriving the normalized maximum deflection as $\mathrm{Max}\overline{u}_y = \frac{\mathrm{Max}u_y}{\varphi_t} = cL^3$, with $c = \frac{F}{12\pi E\varphi_f^4\varphi_t}$ and $L = \frac{1}{2}d + \frac{1}{2}\varphi_b$, where F is the transverse force (see Fig. 1c), E is the elastic modulus of carbon fibre, d is the distance between neighbouring beads, φ_b is the diameter of bead, φ_f is the diameter of carbon fibre cathode, and φ_t is the inner diameter of tube. When considering $E = 228$GPa , $\varphi_t = 8$mm , the possible deflection of bead is described at different F in Fig. 1c. It is found that the normalized maximum deflection is less than 0.002 (~16 µm off the central line) when L is up to 20 mm, which is less than 2 % of the remaining gap between bead and inner wall. Accordingly, the following experiments utilise hybrid cathode with $L = 20$ mm, otherwise specifically stated. Such a design offers a flexible cathode to follow the electrolyte flow while ensuring good stabilization of the cathode at the coaxial position (Fig. 1d) to fulfil a uniform anodization layer on surface (Figure S1), regardless of the structural deformation (Fig. 1e).
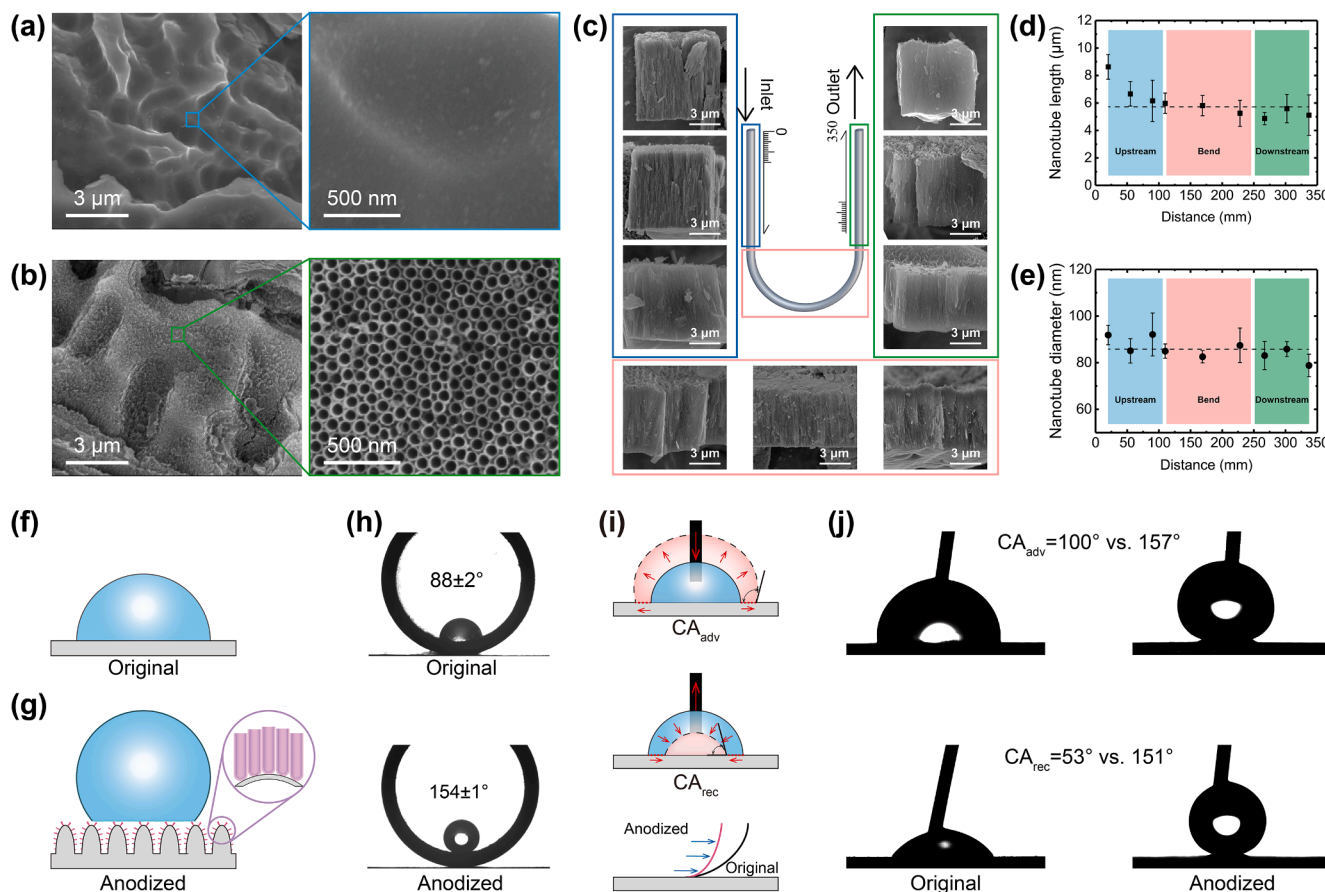
We next measure the length of anodized nanotubes in a straight tube (100 mm long) to verify the distribution of electric field at different locations, e.g., at the upstream (i.e., prior to the bead) and downstream (i.e., after the bead) regions under different flow rates (about 10 mm away from the bead). In Fig. 1f, it is found that, regardless of the position examined, the nanotube length increases with the flow rate and reaches a maximum at 55 mL min⁻¹, because of the accelerated ion feeding; thereafter, it drops gradually, due to the enhanced chemical etching rate of the early-formed nanotubes [33,34]. At the same flow rate, the length of nanotube at the upstream region is longer than that at the downstream section, which can be attributed to sufficient supply of ionic component in a fresher electrolyte solution. It should be noted that the nanotubes grown at the bead position exhibit the largest growth rate. There are two major reasons: firstly, the lines of electric field are bent in the vicinity of bead, lowering the effective field across the oxide layer [28,33]. Secondly, the streamlines are concentrated along the bead profile in light of the narrowed cross-sectional area, promoting the ion feeding under the large flow rate. The latter point plays an important

role during the growth process of anodic TiO₂ nanotubes as identified in the previous report [35].

We further investigate the influence of multiple beads on growth of nanotubes (Fig. 1g). The nanotubes grown between two beads exhibit a similar varying trend and seem more stable than single bead (cf. Fig. 1f), where the length deviation becomes less affected by the flow rate. Moreover, the nanotube length falls in the same scale under the same flow rate. Detailed examination suggests that the coating uniformity is merely affected by the beads (Figure S2), hence setting the basis for tailoring the coatings inside deformed tubes. A thin layer of nanograsses is formed at the nanotube surface, due to the dissolution of nanotube tops during the anodization which could be removed by ultrasonic cleaning [36].

A U-shaped tube (bending angle of 180°) is selected to investigate the coaxial anodization performance since the electrolyte flow experiences a severe interaction during the U-turn. By using a structural cathode ($d = 19.5$ mm) to anodize the inner surface of a U-shaped tube, highly ordered nanotube arrays are formed, as compared in Fig. 2a and 2b. (Fig. 3) The cross-sectional FESEM images reveal a uniform distribution of nanotube coating throughout the inner surface of U-shaped tube, as shown in Fig. 2c. An optimal flow rate of 75 mL min⁻¹ was selected based on the macroscopic appearance of the coatings, as shown in Figure S3. An average length of about 5.8 µm (Fig. 2d) and average diameter of round 85 nm (Fig. 2e) are obtained. In principle, the surface morphology plays a key role in affecting the surface wettability (Fig. 2f and 2 g), thus determining the drag reduction. Notably, the surface roughness (Figure S4) increases explicitly from less than 1 ± 0.5 µm for original surface to $\sim 10 \pm 3$ µm for the hierarchical surface after anodization. In this case, the anodized surface shows a super-hydrophobic feature with a static contact angle of 154° (Fig. 2h) upon 1H,1H,2H,2H-Perfluorodecyltriethoxysilane treatment, compared with a hydrophilic state (CA ~ 88°) for the original (un-anodized) surface. To reach the merit for effective drag reduction, it is essential to equip the surface with both a high static CA and a small contact angle hysteresis (CAH, Fig. 2i) [37–39]. In this work, we find that the original surface displays a high contact angle hysteresis of around 47°, whereas a very small CAH of around 6° is detected for the anodized surface. After depositing a water droplet (7 µL) inside a tube, the droplet slips instantly off the anodized surface due to the superhydrophobicity, instead of

Fig. 2. Observation of hierarchical structure and wetting characterization. Top-view FESEM images on the inner surfaces of original a) and anodized b) tubes with magnified view for the selected areas. c) The FESEM observations on the cross section of anodized U-shaped tube for different positions along the tube. Evaluation of anodized TiO_2 nanotubes at the inner surface along a U-shaped tube with d) length and e) diameter. Illustrations f, g) and wetting results on original and anodized surfaces with h) static contact angle values. Illustrations i) of contact angle hysteresis (CAH) and the liquid/substrate contact during the liquid transportation, and the CAH data j) on original and anodized surfaces.
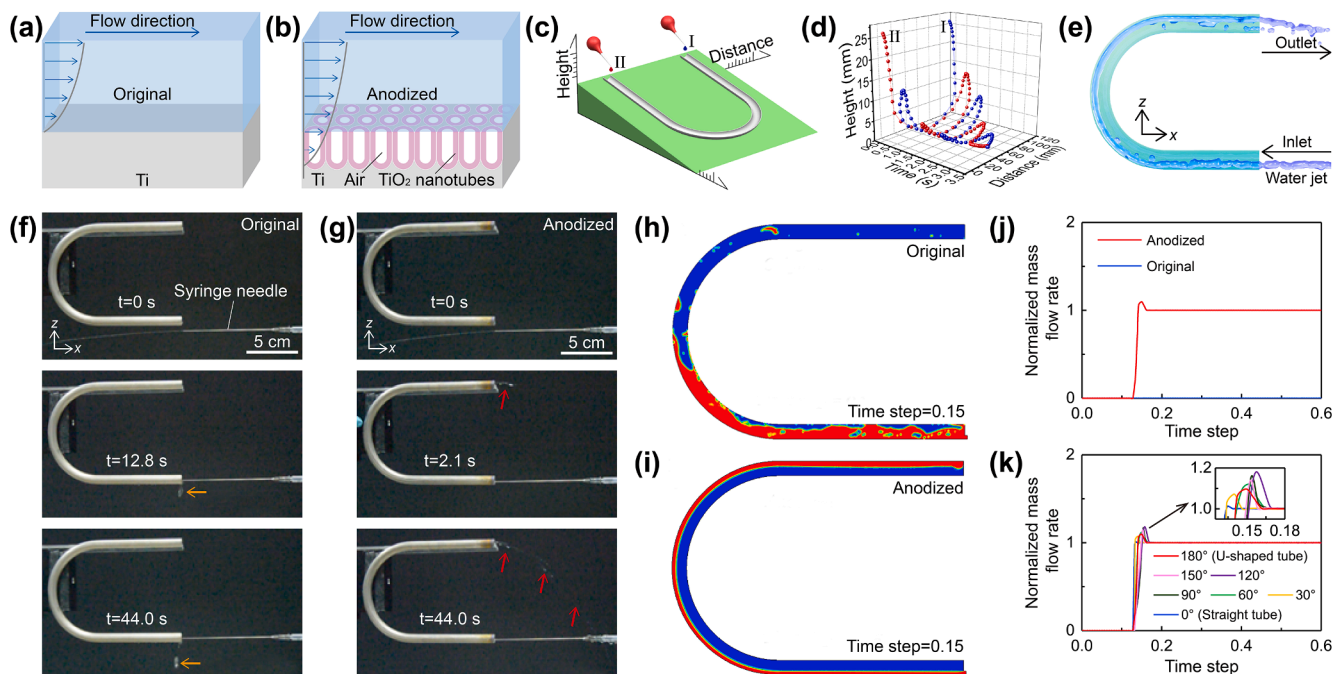
firmly adhering to the original surface (see movie S1).

The liquid/substrate interaction during the liquid transportation has been well understood by a slip boundary layer theory [7,40,41], as shown in Fig. 3a and 3b. We next performed droplet sliding experiment to verify the uniformity of superhydrophobic coating and their impact on the liquid/substrate interaction, by depositing a water droplet into a tilting positioned (~10°) U-shaped tube with both ends levelling at the same height (Fig. 3c) and tracking the sliding trajectory of droplet (movie S2) starting from one end at a time. For the tube with original surface, the water droplet firmly sticks to where it is initially deposited, due to the large CAH value. However, the droplet instantly rolls off once being deposited on the anodized superhydrophobic surface, and presents an oscillating motion (Fig. 3d) until eventually stops at the middle point (lower point), which reflects a good drag reduction by offering a long travel distance along the tube. In addition, the sliding trajectory plots for water droplets departing from different ends show a good symmetry, which indicate a good uniformity of the superhydrophobic coating along the axial direction.

We next study the drag reduction at the anodized surface by pumping a continuous water stream (~27.4 mL min^{-1}) alongside the inner wall of a vertically placed U-shaped tube, with the outlet being located higher than the inlet (Fig. 3e). For the U-shaped tube with original surface, the water stream is unable to pass through and eventually dripped out from the inlet end at 12.8 s (Fig. 3f). Interestingly, the water stream can successfully transport through the anodized U-shaped tube at the same flow rate in just 2.1 s (Fig. 3g). It should be noted that a water fall can be observed out of the upper outlet when the exiting stream stabilizes (see

movie S3), indicating that the stream travels along the super-hydrophobic surface with minimal energy loss. The anodized super-hydrophobic surface consisting of nanotubes and its trapped air (note that the nanotube structure keeps almost unchanged upon PTES treatment, cf. Figure S5), offers a slip interface, thus reduces the frictional drag at the liquid/solid interface.

The finite element (FE) simulation results further confirm the experimental observations about the effect of surface condition. In the case of original surface (Fig. 3h), due to the drag at the surface, the water stream cannot overcome the gravity, especially at the bending region. Consequently, a jamming stream forms at the bottom part of the tube, shown by the red region in Fig. 3h where the volume fraction of water is 100%. The upper part of the tube contains almost no water, as demonstrated by the blue region in Fig. 3h with 0% volume fraction of water. On the contrary, under the same inlet velocity, for the anodized surface with much less frictional drag (Fig. 3i), the water stream can easily overcome the gravity and flow throughout the tube, as shown by a smooth water stream (red line) near the inner surface of the tube in Fig. 3i (see Figure S6 for more simulated phase plots for tubes with different bending degrees).

The numerical results from the FE simulation also quantifies the drag reduction by plotting the normalised mass flow rate (i.e., mass flow rate at the outlet of the tube divided by that at the inlet) as a function of time step for the U-shaped tube (bending angle of 180°) and tubes with other bending angles, which shows a good agreement with the experiment results. For the U-shaped tube (Fig. 3j), under the original surface condition, the normalised mass flow rate is always zero, which means there

Fig. 3. Evaluation of the drag during the liquid/substrate interaction. Diagrams of the flow/substrate interactions on the original a) and anodized b) surfaces. c) Experimental setup of tracking droplet slipping motion in an anodized U-shaped tube. d) Sliding trajectories of two droplets starting from different ends of a superhydrophobic U-shaped tube. e) Illustration of using an aqueous jet flow to track the surface drag reduction in a U-shaped tube. Surface drag reduction testing by pumping an aqueous stream through U-shaped tubes with original f) and anodized g) surfaces, and the corresponding phase plots from finite element simulation for the original h) and anodized i) U-shaped tubes. The normalised mass flow rate as a function of time step for U-shaped tubes j) and deformed tubes with various bending degrees (anodized tube only) k).

is no stream discharge from the outlet. However, in the anodized case, the stream starts to discharge from the outlet of the tube at around 0.13 time step, as shown by a jump of the normalized mass flow rate from 0 to 1 in Fig. 3j. It is noted that the peak mass flow rate (>1) at 0.13 time step is due to the jamming of the liquid transportation. Fig. 3k is for the anodized tubes with bending angles ranging from 0° to 180°. It is found from the figure that the water discharge time is almost the same for all the bending angles, indicating the minor effect of bending angle with respect to the surface condition. The detailed maps of volume fraction of water for all bending angles are shown in Figure S6 (Supporting Information), where the smooth water stream (red line) near the inner surface of the tube is found for all bending angles.

We then evaluate the drag reduction performance of the tubes with anodized surface, in a constant throughout flow setup (Fig. 4a, see Figure S7 for the complete setup). Finite element simulation is also performed to understand the flow conditions when the liquid is transported in the tubes with original or anodized surface. The obtained contour maps of flow rate are shown in Fig. 4b. For the original surface, the highest flow rate is found at the centre and the flow rate decreases to 0 when approaching the tube surfaces, due to the large frictional drag at the surface. On the contrary, for the anodized surface of little surface drag, a relatively uniform distribution of flow rate is found. The finite element simulations of other levels of constant inlet flow are also performed, and the obtained contour maps of flow rate at low inlet flow (1 m s^{-1}) and high inlet flow (5 m s^{-1}) are shown in Figure S8 (Supporting Information), where the relatively uniform distribution of flow rate is also found for the anodized surfaces.
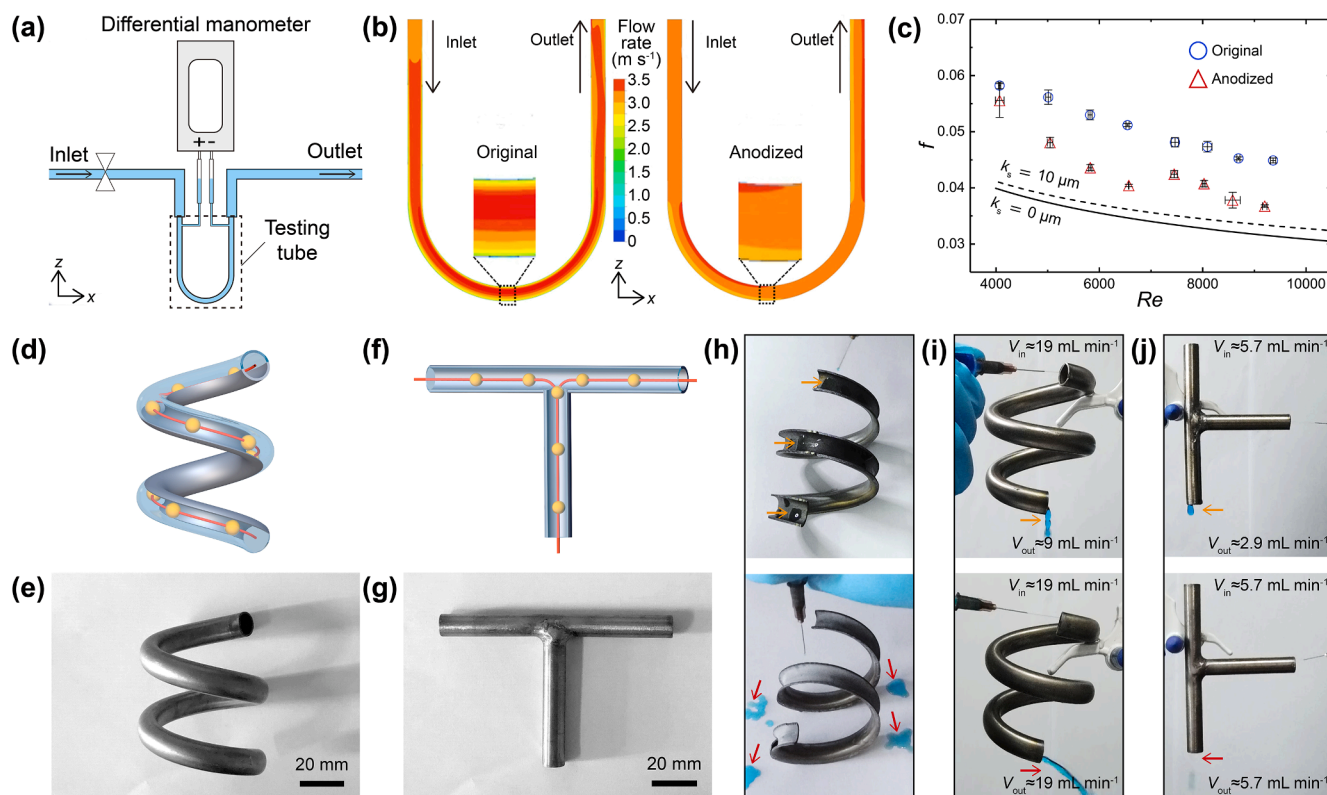
The further numerical analysis focuses on the high Reynolds number (Re > 4000) region/turbulent regime, since it has been a challenging topic to get accurate and repeatable results in the laminar regime with the constant head lab setup and turbulent regime has been the major concern for energy consumption of liquid transportation in industrial applications [42,43]. The analytical friction factor is derived from Colebrook formula [44,45] as $\frac{1}{f^{0.5}} = -2.0 log10(\frac{k_s/\varphi_t}{3.7} + \frac{2.51}{Ref^{0.5}})$ and $Re =$

$\frac{2.51}{f^{0.5}(10^{-\frac{1}{2.0f^{0.5}}} - \frac{k_s/\varphi_t}{3.7})}$, where k_s/φ_t is the relative roughness and φ_t is the diameter of tube. The friction factor can be calculated as $f = \frac{\rho\pi^2 t^2 \varphi_t^5 \Delta P}{8Lm^2}$ with experimental data, where ρ is the density of water, $\varphi_t = 8$ mm, $t = 20$ s, $L = 330$ mm, m is the mass of water, and ΔP is the differential pressure.

The friction factors extracted from the Colebrook formula and experiments at $Re > 4000$ are summarised in Fig. 4c, for the tubes with original and anodized surface. For an increasing flow velocity, the friction factor presents a declining trend for each curve over the entire range. Moreover, the anodized surface presents up to 25.8% drag reduction, due to the generation of plastron lubricating the flow of water over the anodized surface. It is noteworthy that the friction factor of the U-shaped surface at each Reynolds number is higher than that of the value determined by the Colebrook formula. This is reasonable, considering that the formula is applicable for straight pipes with smaller fraction factor than bend counterparts. Above data show a reduced drag in the anodized tube when compared to the original tube, in good agreement with the theoretical prediction.

We further apply the coaxial anodization to the tubes with more complicated deformations, a spiral tube (Fig. 4d and 4e) and a T-junction (Fig. 4f and 4 g). A quick verification of the formation of hydrophobic layer on the surface is conducted by depositing the water droplets on the inner surface of spiral tube (movies S4), where we find that the water droplet slips instantly off the anodized tube (Fig. 4h). By pumping a continuous water stream in the setup as shown in Fig. 4i and 4j, almost zero energy loss is observed for the anodized surface (movies S5-S6), in contrast to the significant reductions on the flow rate for the original surface. The coaxial anodization can be operated in a flexible fashion to fulfil a conformal hydrophobic coating (movie S7), thus enabling drag reduction in deformed tube with a promising application in wide engineering system (see Figure S9). However, the actual mechanism could be very complicated and affected by more varied factors such as impact, bouncing, gravity, and so on, which will be

Fig. 4. The drag reduction of the constant throughout flow and the demonstration of applying coaxial anodization in the deformed tube with complicated shapes. Illustration of the constant flow testing setup to assess the drag reduction of liquid transportation in a U-shaped tube a), with finite element simulation results b). c) The analytical and experimental results on the friction factor (*f*) *versus* Reynolds number (*Re*). Illustration of anodizing d) a spiral tube with an image of anodized product in e), and f) a T-junction with an image of anodized product in g). h) Demonstration of the interaction between liquid and inner wall in spiral tube by depositing droplets on original (top) and anodized inner surface (bottom). Surface drag reduction testing by pumping an aqueous stream to pass through the original (top) and anodized (bottom) spiral tube i) and T-junction j).

investigated further in the future work. The stability of the nanostructured coatings and the superhydrophobic states is also of key concern for engineering application, which is demonstrated under continuous water flow in terms of laminar and turbulent condition, as displayed in Figures S10-S17.

4. Conclusions

In summary, we describe a facile anodization strategy to achieve uniform distribution of hierarchical structure within deformed Ti tubes, in a controllable and self-adaptive manner. The hybrid cathode design can self-stabilise at a wild range of flow rate without explicit deflection, to create a uniform and superhydrophobic TiO_2 nanotube layer at the inner surface of tubes with minimal contact angle hysteresis. As such, a significant drag reduction is facilitated on the hydrophobic nanostructured surface, where both the experimental and theoretical results show that skin friction has been minimised. Interestingly, the liquid flow can be transported through the U-shaped tube freely regardless of the bending degree and shape of tube. The formation of plastron lubricating the flow of water over the anodized surface leads to an apparent slip layer and reduction in the average shear stress acting on the flow.

Declaration of Competing Interest

The authors declare that they have no known competing financial interests or personal relationships that could have appeared to influence the work reported in this paper.

Appendix A. Supplementary data

Supplementary data to this article can be found online at https://doi.org/10.1016/j.cej.2021.133746.

References

[1] J.K. Swanepoel, W.G. le Roux, A.S. Lexmond, J.P. Meyer, Helically coiled solar cavity receiver for micro-scale direct steam generation, Appl. Therm. Eng. 185 (2021) 116427, https://doi.org/10.1016/j.applthermaleng.2020.116427.

[2] A.M. Fsadni, J.P.M. Whitty, A review on the two-phase heat transfer characteristics in helically coiled tube heat exchangers, Int. J. Heat. Mass. Tran. 95 (2016) 551–565, https://doi.org/10.1016/j.ijheatmasstransfer.2015.12.034Get.

[3] G. Jian, S. Wang, L. Sun, J. Wen, Numerical investigation on the application of elliptical tubes in a spiral-wound heat exchanger used in LNG plant, Int. J. Heat. Mass. Tran. 130 (2019) 333–341, https://doi.org/10.1016/j.ijheatmasstransfer.2018.10.089Get.

[4] C.-H. Qi, H.-J. Feng, Q.-C. Lv, Y.-L. Xing, N. Li, Performance study of a pilot-scale low-temperature multi-effect desalination plant, Appl. Energy 135 (15) (2014) 415–422, https://doi.org/10.1016/j.apenergy.2014.08.096.

[5] G.O. Prado, L.G.M. Vieira, J.J.R. Damasceno, Solar dish concentrator for desalting water, Sol. Energy 136 (15) (2016) 659–667, https://doi.org/10.1016/j.solener.2016.07.039.

[6] B.B. Kanbur, C. Wu, S. Fan, W. Tong, F. Duan, Two-phase liquid-immersion data center cooling system: experimental performance and thermoeconomic analysis, Int. J. Refrig. 118 (2020) 290–301, https://doi.org/10.1016/j.ijrefrig.2020.05.026.

[7] J.P. Rothstein, Slip on superhydrophobic surfaces. Annu. Rev. Fluid Mech. 42 (2010) 89-109. https://doi.org/ 10.1146/annurev-fluid-121108-145558.

[8] E. Aljallis, M.A. Sarshar, R. Datla, V. Sikka, A. Jones, C.-H. Choi, Experimental study of skin friction drag reduction on superhydrophobic flat plates in high reynolds number boundary layer flow, Phy. Fluids 25 (2) (2013) 025103, https://doi.org/10.1063/1.479160210.1063/1.4791602.110.1063/1.4791602.2.

[9] M. Vuckovac, M. Backholm, J.V.I. Timonen, R.H.A. Ras, Viscosity-enhanced droplet motion in sealed superhydrophobic capillaries, Sci. Adv. 6 (42) (2020) eaba5197, https://doi.org/ 10.1126/sciadv.aba5197.

[10] G. McHale, M.R. Flynn, M.I. Newton, Plastron induced drag reduction and increased slip on a superhydrophobic sphere, Soft Matter 7 (2011) 10100–10107, https://doi.org/10.1039/C1SM06140B.

[11] D. Daniel, J.V.I. Timonen, R. Li, S.J. Velling, J. Aizenberg, Oleoplaning droplets on lubricated surfaces, Nat. Phys. 13 (10) (2017) 1020–1025, https://doi.org/10.1038/nphys4177.

[12] I.U. Vakarelsk, J.O. Marston, D.Y. Chan, S.T. Thoroddsen, Drag reduction by leidenfrost vapor layers, Phys. Rev. Lett. 106 (2011), 214501, https://doi.org/10.1103/PhysRevLett.106.214501.

[13] J. de Ruiter, R. Lagraauw, D. van den Ende, F. Mugele, Wettability-independent bouncing on flat surfaces mediated by thin air films, Nat. Phys. 11 (1) (2015) 48–53, https://doi.org/10.1038/nphys3145.

[14] D. Saranadhi, D. Chen, J.A. Kleingartner, S. Srinivasan, R.E. Cohen, G.H. McKinley, Sustained drag reduction in a turbulent flow using a low-temperature leidenfrost surface. Sci. Adv. 2 (10) (2016) e1600686. https://doi.org/ 10.1126/sciadv.1600686.

[15] L.E. Dodd, P. Agrawal, M.T. Parnell, N.R. Geraldi, B.B. Xu, G.G. Wells, S. Stuart-Cole, M.I. Newton, G. McHale, D. Wood, Low-friction self-centering droplet propulsion and transport using a leidenfrost herringbone-ratchet structure, Phys. Rev. Appl. 11 (3) (2019), https://doi.org/10.1103/PhysRevApplied.11.034063.

[16] A.A. Dev, R. Dey, F. Mugele, Behaviour of flexible superhydrophobic striped surfaces during (electro-)wetting of a sessile drop, Soft Matter 15 (48) (2019) 9840–9848.

[17] H. Tan, S. Wooh, H.J. Butt, X. Zhang, D. Lohse, Porous supraparticle assembly through self-lubricating evaporating colloidal ouzo drops, Nat. Commun. 10 (2019) 478, https://doi.org/10.1038/s41467-019-08385-w.

[18] M. Vuckovac, M. Backholm, J.V.I. Timonen, R.H.A Ras, Viscosity-enhanced droplet motion in sealed superhydrophobic capillaries. Sci. Adv. 6 (42) (2020) eaba5197. https://doi.org/ 10.1126/sciadv.aba5197.

[19] H. Hu, J. Wen, L. Bao, L. Jia, D. Song, B. Song, G. Pan, M. Scaraggi, D. Dini, Q. Xue, F. Zhou, Significant and stable drag reduction with air rings confined by alternated superhydrophobic and hydrophilic strips, Sci. Adv. 3 (9) (2017) e1603288. https://doi.org/ 10.1126/sciadv.1603288.

[20] R. Truesdell, A. Mammoli, P. Vorobieff, F. van Swol, C.J. Brinker, Drag reduction on a patterned superhydrophobic surface, Phys. Rev. Lett. 97 (2016), 044504, https://doi.org/10.1103/PhysRevLett.97.044504.

[21] F.M. White, Fluid Mechanics, five ed., McGraw-Hill, New York, 2011.

[22] S. Gogte, P. Vorobieff, R. Truesdell, A. Mammoli, F. van Swol, P. Shah, C.J. Brinker, Effective slip on textured superhydrophobic surfaces, Phys. Fluids 17 (5) (2005) 051701, https://doi.org/10.1063/1.1896405.

[23] S. Wang, K. Liu, X. Yao, L. Jiang, Bioinspired surfaces with superwettability: new insight on theory, design, and applications, Chem. Rev. 115 (16) (2015) 8230–8293, https://doi.org/10.1021/cr400083y.

[24] H. Zhang, X. Zeng, Y. Gao, F. Shi, P. Zhang, J.-F. Chen, A facile method to prepare superhydrophobic coatings by calcium carbonate, Ind. Eng. Chem. Res. 50 (6) (2011) 3089–3094, https://doi.org/10.1021/ie102149y.

[25] K. Watanabe, Y. Udagawa, H. Udagawa, Drag reduction of newtonian fluid in a circular pipe with a highly water-repellent wall, J. Fluid Mech. 381 (1999) 225–238, https://doi.org/10.1017/S0022112098003747.

[26] J.-J. Yuan, R.-H. Jin, Water motion and movement without sticking, weight loss and cross-contaminant in superhydrophobic glass tube, Nanotechnology 21 (6) (2010) 065704, https://doi.org/10.1088/0957-4484/21/6/065704.

[27] F.Y. Lv, P. Zhang, Drag reduction and heat transfer characteristics of water flow through the tubes with superhydrophobic surfaces, Energy Conv. Manag. 113 (2016) 165–176, https://doi.org/10.1016/j.enconman.2016.01.034.

[28] L. Sun, X. Wang, M. Li, S. Zhang, Q. Wang, Anodic titania nanotubes grown on titanium tubular electrodes, Langmuir 30 (10) (2014) 2835–2841, https://doi.org/10.1021/la500050q.

[29] C. Xiang, L. Sun, Y.e. Wang, G. Wang, X. Zhao, S. Zhang, Large-scale, uniform, and superhydrophobic titania nanotubes at the inner surface of 1000 mm long titanium tubes, J. Phys. Chem. C 121 (28) (2017) 15448–15455, https://doi.org/10.1021/acs.jpcc.7b0312410.1021/acs.jpcc.7b03124.s00110.1021/acs.jpcc.7b03124.s00210.1021/acs.jpcc.7b03124.s00310.1021/acs.jpcc.7b03124.s00410.1021/acs.jpcc.7b03124.s00510.1021/acs.jpcc.7b03124.s006.

[30] C. Xiang, L. Sun, General way to compute the intrinsic contact angle at tubes, J. Phys. Chem. C 122 (51) (2018) 29210–29219, https://doi.org/10.1021/acs.jpcc.8b0810010.1021/acs.jpcc.8b08100.s001.

[31] C. Xiang, X. Zhao, L. Tan, J. Ye, S. Wu, S. Zhang, L. Sun, A Solar tube: efficiently converting sunlight into electricity and heat, Nano Energy 55 (2019) 269–276, https://doi.org/10.1016/j.nanoen.2018.10.077.

[32] H. Li, M. Ding, J. Jin, D. Sun, S. Zhang, C. Jia, L. Sun, Effect of electrolyte pretreatment on the formation of TiO$_2$ nanotubes: an ignored yet non-negligible factor, ChemElectroChem 5 (2018) 1006–1012. https://doi.org/ 10.100 2/celc.201800240.

[33] L. Sun, S. Zhang, X.W. Sun, X. Wang, Y. Cai, Double-sided anodic titania nanotube arrays: a lopsided growth process, Langmuir 26 (23) (2010) 18424–18429, https://doi.org/10.1021/la103390s.

[34] L. Sun, S. Zhang, X. Wang, X.W. Sun, D.Y. Ong, A.K.K. Kyaw, A novel parallel configuration of dye-sensitized solar cells with double-sided anodic nanotube arrays, Energy Environ. Sci. 4 (2011) 2240–2248, https://doi.org/10.1039/C1EE01196K.

[35] K. Syrek, J. Kapusta-Kolodziej, M. Jarosz, G.D. Sulka, Effect of electrolyte agitation on anodic titanium dioxide (ATO) growth and its photoelectrochemical properties, Electrochim. Acta 180 (2015) 801–810, https://doi.org/10.1016/j.electacta.2015.09.011.

[36] L. Sun, S. Zhang, X. Wang, X.W. Sun, D.Y. Ong, X. Wang, D. Zhao, Transition from anodic titania nanotubes to nanowires: arising from nanotube growth to application in dye-sensitized solar cells, ChemPhysChem 12 (18) (2011) 3634–3641, https://doi.org/10.1002/cphc.v12.1810.1002/cphc.201100450.

[37] J. Hui Guan, É. Ruiz-Gutiérrez, B.B. Xu, D. Wood, G. McHale, R. Ledesma-Aguilar, G. George Wells, Drop transport and positioning on lubricant-impregnated surfaces, Soft Matter 13 (18) (2017) 3404–3410, https://doi.org/10.1039/C7SM00290D.

[38] N.R. Geraldi, J.H. Guan, L.E. Dodd, P. Maiello, B.B. Xu, D. Wood, M.I. Newton, G.G. Wells, G. McHale, Double-sided slippery liquid-infused porous materials using conformable mesh, Sci. Rep. 9 (2019) 13280, https://doi.org/10.1038/s41598-019-49887-3.

[39] S. Peppou-Chapman, J.K. Hong, A. Waterhouse, C. Neto, Life and death of liquid-infused surfaces: a review on the choice, analysis and fate of the infused liquid layer, Chem. Soc. Rev. 49 (11) (2020) 3688–3715, https://doi.org/10.1039/D0CS00036A.

[40] C.-H. Choi, C.-J. Kim, Large slip of aqueous liquid flow over a nanoengineered superhydrophobic surface, Phys. Rev. Lett. 96 (6) (2006) 066001, https://doi.org/10.1103/PhysRevLett.96.066001.

[41] C. Lee, C.-H. Choi, C.-J. Kim, Superhydrophobic drag reduction in laminar flows: a critical review, Exp. Fluids 57 (2016) 176, https://doi.org/10.1007/s00348-016-2264-z.

[42] B. Vajdi Hokmabad, S. Ghaemi, Turbulent flow over wetted and non-wetted superhydrophobic counterparts with random structure, Phys. Fluids 28 (1) (2016) 015112, https://doi.org/10.1063/1.4940325.

[43] D. Reholon, S. Ghaemi, Plastron morphology and drag of a superhydrophobic surface in turbulent regime, Phys. Rev. Fluids 3 (10) (2018), 104003, https://doi.org/10.1103/PhysRevFluids.3.104003.

[44] C.F. Colebrook, T. Blenc, H. Chatley, E.H. Essex, J.R. Finnecome, G. Lacey, J. Williamson, G.G. Macdonald, Turbulent flow in pipes, with particular reference to the transition between the smooth and rough pipe laws, J. Inst. Civ. Eng. 12 (8) (1939) 393–422, https://doi.org/10.1680/ijoti.1939.14509.

[45] N.R. Geraldi, L.E. Dodd, B.B. Xu, G.G. Wells, D. Wood, M.I. Newton, G. McHale, Drag reduction properties of superhydrophobic mesh pipes, Surf. Topogr. Metrol. Prop. 5 (3) (2017) 034001, https://doi.org/10.1088/2051-672X/aa793b.